Study on the Induction Method of Electrical Prospecting

By

Takeshi KIYONO, Koichi KIMURA and Keiichi KOBAYASHI

Department of Mining Engineering

(Received April, 1954)

1. Introduction

There are many kinds of electromagnetic prospecting methods, but the fundamental quantities to be measured in these methods are the amplitude, phase angle and direction of the magnetic field produced by an orebody in the alternating field of an exciting loop. In practice, the resultant vector composed of the primary field of loop and the secondary field due to orebody is observed. However, to interprete these results, it is necessary to know the electromagnetic behaviours of orebodies in the primary field.

In this paper, some of the experimental and theoretical results concerning the electromagnetic induction method are reported. The effects of the electromagnetic properties of spherical orebody on the secondary magnetic field are discussed. The distribution of the field produced by a disc is also clarified theoretically and compared with the experiment.

2. Theoretical Considerations

(1) Secondary field due to a spherical body.

If we assume that (1) the primary field surrounding the sphere is uniform and vertical, (2) the electromagnetic property of the medium surrounding the sphere is similar to that of the air, and (3) the displacement current in the medium and sphere can be ignored for low frequencies, then the three components H_r, H_θ and H_ϕ of the secondary field at an arbitrary point $P(r, \theta, \phi)$ outside the sphere beome as follows (see Fig. 1):

$$\left.\begin{aligned} H_r &= -QH_0\frac{a^3}{r^3}\cos\theta\cos(\omega t+\delta), \\ H_\theta &= -\frac{1}{2}QH_0\frac{a^3}{r^3}\sin\theta\cos(\omega t+\delta), \\ H_\phi &= 0, \end{aligned}\right\} \qquad (1)$$

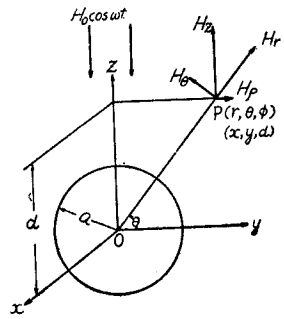

Fig. 1.

where ω denotes the angular frequency of the field, a, σ and μ are radius, conductivity and permeability of the sphere respectively. And the primary field is expressed by $H_0 \cos \omega t$.

The factor Q and phase angle δ in Eq. (1) are given by

$$Q = \sqrt{X^2+Y^2} \tag{2}$$

and

$$\delta = \tan^{-1}(Y/X), \tag{3}$$

where

$$\begin{aligned} X = -\frac{1}{\Delta}\Big[&(1-\mu)(1-2\mu)\Big\{\frac{1}{2}(\cosh 2p-\cos 2p)-p(\sinh 2p+\sin 2p) \\ &+p^2(\cosh 2p+\cos 2p)\Big\}-p^3(2+\mu)(\sinh 2p-\sin 2p) \\ &+2p^4(\cosh 2p-\cos 2p)\Big], \end{aligned} \tag{4}$$

$$Y = \frac{3\mu p^2}{\Delta}\Big\{(\cosh 2p-\cos 2p)-p(\sinh 2p+\sin 2p)\Big\}, \tag{5}$$

$$\begin{aligned} \Delta = &(1-\mu)^2\Big\{\frac{1}{2}(\cosh 2p-\cos 2p)-p(\sinh 2p+\sin 2p)+p^2(\cosh 2p+\cos 2p)\Big\} \\ &-2(1-\mu)p^3(\sinh 2p-\sin 2p)+2p^4(\cosh 2p-\cos 2p), \end{aligned} \tag{6}$$

and

$$p = (a/c)\sqrt{2\pi\omega\mu\sigma}. \tag{7}$$

From Eq. (1), we obtain the following expressions for the horizontal and vertical components of the secondary field:

$$H_\rho = -\frac{m}{r^5}3\rho d, \tag{8}$$

$$H_z = -\frac{m}{r^5}(\rho^2-2d^2), \tag{9}$$

where

$$\rho = \sqrt{x^2+y^2} \tag{10}$$

and

$$m = \frac{1}{2}QH_0a^3\cos(\omega t+\delta). \tag{11}$$

Fig. 2 shows the distribution of the secondary field calculated from Eqs. (8) and (9).

From the above expressions, it can be seen that the secondary field by the sphere is equal to that of the magnetic dipole which is placed at the center of the sphere and the moment of which is m in Eq. (11). Substituting Eqs. (2) and (3) into (11), we get

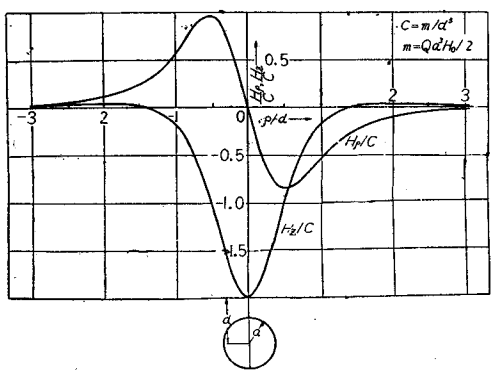

Fig. 2. Secondary field due to a spherical consuctor.

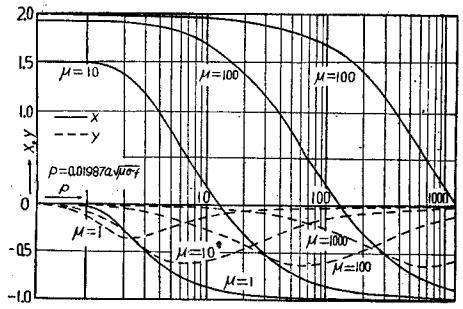

Fig. 3.

$$m=\frac{1}{2}H_0a^3(X+iY)e^{i\omega t},\quad Qe^{i\delta}=X+iY. \tag{12}$$

As the frequency, conductivity and permeability are included in X and Y, we can assume their effects on the secondary field as the effects on the function X and Y. Fig. 3 shows the real part X and imaginary part Y of $Qe^{i\delta}$ as functions of p and for various values of permeability μ.

(2) Secondary field due to an oblate spheroid.

The assumptions made in the treatment of the field of a sphere hold also for a spheroid. In addition, we assume, for the sake of simplicity, that the conductivity of the spheroid is infinite. In such a case the expressions for the components of secondary field at the point (λ, μ, ϕ) become as follows,

$$\left.\begin{aligned} H_\lambda &= -H_0\frac{\sqrt{\lambda_0^2+1}}{Q_1^1(i\lambda_0)}\frac{\mu}{\sqrt{\lambda^2+\mu^2}}Q_1^1(i\lambda)\cos\omega t,\\ H_\mu &= -H_0\frac{\sqrt{\lambda_0^2+1}}{Q_1^1(i\lambda_0)}\sqrt{\frac{1-\mu^2}{\lambda^2+\mu^2}}Q_1(i\lambda)\cos\omega t,\\ H_\phi &= 0, \end{aligned}\right\} \tag{13}$$

where λ, μ, ϕ are the oblate spheroidal coordinates as shown in Fig. 4, and λ_0 is the parameter for the surface of spheroidal conductor. The relation between λ, μ, ϕ and the rectangular coordinates x, y, z is given by

$$\left.\begin{aligned} x &= c\sqrt{\lambda^2+1}\,\sqrt{1-\mu^2}\cos\phi,\\ y &= c\sqrt{\lambda^2+1}\,\sqrt{1-\mu^2}\sin\phi,\\ z &= c\lambda\mu, \end{aligned}\right\} \tag{14}$$

where c is the distance between the center and a focus.

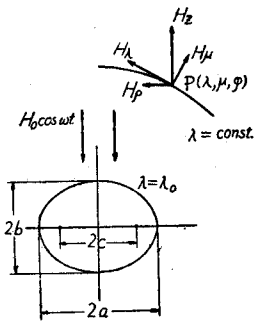

Fig. 4.

Let $2a$ and $2b$ be major and minor axes of the spheroid, then

$$\left.\begin{aligned} c &= \sqrt{a^2-b^2}\,, \\ \lambda_0 &= b/c\,. \end{aligned}\right\} \tag{15}$$

If we let λ_0 be zero, the spheroid degenerates to a disc of radius a. For this limiting case, Eq. (13) becomes as follows:

$$\left.\begin{aligned} H_\lambda &= -H_0\frac{2}{\pi}\frac{\mu}{\sqrt{\lambda^2+\mu^2}}Q_1^1(i\lambda)\cos\omega t\,, \\ H_\mu &= -H_0\frac{2}{\pi}\sqrt{\frac{1-\mu^2}{\lambda^2+\mu^2}}Q_1(i\lambda)\cos\omega t\,. \end{aligned}\right\} \tag{16}$$

The Legendre functions of the second kind included in these equations, are

$$\left.\begin{aligned} Q_1(i\lambda) &= \lambda\cot^{-1}\lambda - 1\,, \\ Q_1^1(i\lambda) &= \sqrt{\lambda^2+1}\cot^{-1}\lambda - \frac{\lambda}{\sqrt{\lambda^2+1}}\,. \end{aligned}\right\} \tag{17}$$

The horizontal and vertical components of the field produced by a disc can be deduced from Eq. (16):

$$\left.\begin{aligned} H_\rho &= -H_0\frac{2}{\pi}\sqrt{\frac{1-\mu^2}{\lambda^2+1}}\frac{\mu}{\lambda^2+\mu^2}\cos\omega t\,, \\ H_z &= -H_0\frac{2}{\pi}\left(\cot^{-1}\lambda - \frac{\lambda}{\lambda^2+\mu^2}\right)\cos\omega t\,. \end{aligned}\right\} \tag{18}$$

Figs. 5 and 6 show the radial distribution of the horizontal and vertical compoent of the secondary field produced by a horizontal disc of perfect conductor at various depths.

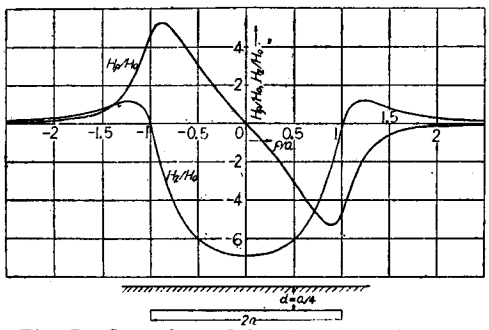

Fig. 5. Secondary field due to a disc of perfect conductor (1).

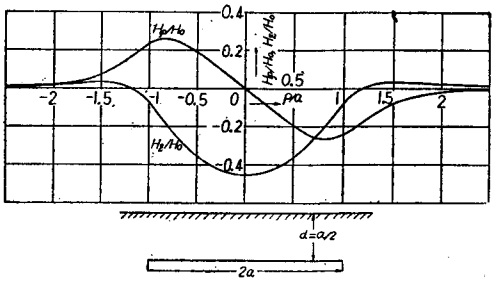

Fig. 6. Secondary fiield due to a disc of perfect conductor (2).

3. Experimental Research

In this experiment, the relative amplitude and phase angle of the vertical component of resultant field are measured. These quantities are obtained on the basis

of the primary field at the center of a square loop which produces the exciting field.

The frequencies used in this experiment are 250, 500, 1,000, 2,000, 5,000 and 10,000 c/s, and the models for orebodies are as follows:

Material	Shape	Radius in mm	Thickness in mm
Copper	Disc	56	0.5, 1.0, 2.5, 4.0
Aluminium	Disc	56	1.0
Iron	Disc	56	1.0
Lead	Disc	56	1.0, 4.0
Brass	Sphere	56	—
Cast Iron	Sphere	56	—

Fig. 7 shows the experimental setup. The exciting current flowing in two loops is about 50 mA, and it produces the primary field in the exciting loop, and the standard field at the center of the reference loop.

Measurements are made by the use of an AC potentiometer shown in Fig. 8. The amplitudes of two electromotive forces induced in two equal search coils are compared by means of two potentiometers, and the phase difference between these two electromotive forces is measured by two phase shifting networks using four triodes of the same type.

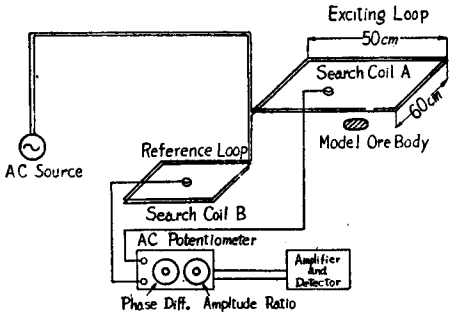

Fig. 7.

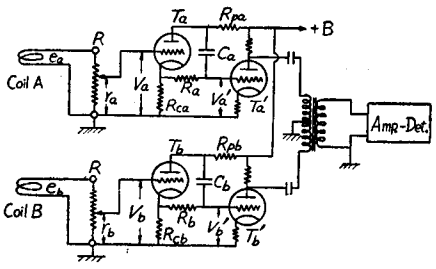

Fig. 8.

In Fig. 8, let μ and r_p be the amplification constant and internal resistance of these triodes, and let r and L be the resistance and self-inductance of search coils respectively, then the voltage V_a' appearing at the grid of triode T_a', can be expressed as follows:

$$V_a' = \frac{\mu}{K}\frac{r_a e_a}{\sqrt{(r+R)^2+\omega^2L^2}}\, e^{i(\theta_a+\theta_a')} \tag{19}$$

where

$$K^2 = (\mu+2+\alpha)^2 + \frac{4\omega^2C_a^2r_p\{r_p+R_a(\mu+2+\alpha)\}}{1+\omega^2C_a^2R_a^2}, \tag{20}$$

$$\alpha = r_p/R_{pa}, \qquad R_{pa} = R_{ca}, \tag{21}$$

$$\theta_a = -\tan^{-1}\frac{\omega L}{r+R}, \tag{22}$$

$$\theta_a' = 2\tan^{-1}\frac{1}{\omega C_a R_a} + \tan^{-1}\frac{\mu+2+\alpha}{\omega C_a[(\mu+2+\alpha)R_a+2r_p]}. \tag{23}$$

In practice, we can make $R_a \gg r_p$, and $1/\omega C_a \gg r_p$, so Eqs. (19) and (23) may be written as follows:

$$V_a' = \frac{\mu}{\mu+2+\alpha}\frac{r_a e_a}{\sqrt{(r+R)^2+\omega^2L^2}}e^{i(\theta_a+\theta_a')} \tag{24}$$

and

$$\theta_a' = 2\tan^{-1} 1/(\omega C_a R_a). \tag{25}$$

On the other hand, the input voltage V_b' of triode T_b' is given by

$$V_b' = \frac{\mu}{\mu+2+\beta}\frac{r_b e_b}{\sqrt{(r+R)^2+\omega^2L^2}}e^{i(\theta_b+\theta_b')}, \tag{26}$$

where

$$\theta_b = -\tan^{-1}\frac{\omega L}{r+R} = \theta_a, \tag{27}$$

$$\theta_b' = 2\tan^{-1} 1/(\omega C_b R_b), \tag{28}$$

and

$$\beta = r_p/R_{pb}, \qquad R_{pb} = R_{cb}. \tag{29}$$

If we make $R_{pa} = R_{ca} = R_{pb} = R_{cb}$, then $\alpha = \beta$.

For the balance condition, $V_a' = V_b'$, then we obtain the relation:

$$\frac{e_a}{e_b} = \frac{r_b}{r_a}e^{i(\theta_a'-\theta_b')}. \tag{30}$$

So that, the amplitude ratio of the field H_a to the reference field H_b, and the phase difference between them are expressed by following equations:

$$\frac{H_a}{H_b} = \frac{r_b}{r_a}, \tag{31}$$

$$\varphi = 2\left(\tan^{-1}\frac{1}{\omega C_b R_b} - \tan^{-1}\frac{1}{\omega C_a R_a}\right). \tag{32}$$

Eq. (32) is obtained assuming that r_p is very small compared with R_a, R_b, $1/\omega C_a$ and $1/\omega C_b$, but in practice, the error owing to this approximation is less than 0°45′ within the frequency range of our experiment.

The values of resistances and capacitances used in the potentiometer of Fig. 8 are:

$$R_{ca} = R_{pa} = R_{cb} = R_{pb} = 3\,\mathrm{k}\Omega\,,$$
$$R_a = 30-50\,\mathrm{k}\Omega\,,$$
$$R_b = 41.8\,\mathrm{k}\Omega\,,$$
$$C_a = C_b = 3.8/f\ \mu\mathrm{F}\,,$$

where f is the frequency in c/s.

The range of amplitude measurement is 0.1 to 1.9, and that of the phase measurement is $-20°$ to $+20°$.

4. Results of Measurements

The amplitude and phase of the secondary field can be calculated from the resultant field by subtracting the primary field vectorially. The secondary field means the anomaly in magnetic field caused by an orebody, and it is affected by the depth and property of the orebody and the frequency of the field. So, we shall classify the results of observations in three groups for the sake of convenience.

(1) The amplitude and phase difference as functions of distance from the center of the exciting loop when the depths of the orebody are varied at a constant frequency ($f = 1{,}000$ c/s).

Figs. 9 and 10 show the fields for copper and lead discs, and Figs. 11 and 12 are for brass and iron spheres. In these figures s means the distance from the center of the loop to the top of the model orebody.

The difference between Figs. 9 and 10 shows the effects of conductivity of orebodies, and the difference between Figs. 11 and 12 shows the influence of permeability on the secondary magnetic field.

The magnetic property of material of a thin disc which lies perpendicular to the uniform primary field does not have much effect upon the secondary magnetic field, because the part of magnetic path occupied by the disc is very short.

(2) The same as (1), but for various frequencies and a constant depth ($s/a=1/4$).

These results are shown in Figs. 13, 14, 15 and 16. It is found that the iron sphere behaves as a magnetic body at lower frequencies, but at higher frequencies it approaches a non-magnetic conductor.

(3) The same as (1), but for various materials and a constant depth ($s/a=1/4$).

Figs. 17 and 18 show the effects of properties of materials on the secondary field. As the frequency becomes higher, the differences between curves for different materials become smaller.

Some of the results of these experiments can be compared with the theoretical curves. In Figs. 19 and 20, the theoretical distributions of vertical anomalies are compared with the experimental data. The primary field produced by a square loop is not perfectly uniform at about the sphere. So that we must take the value at

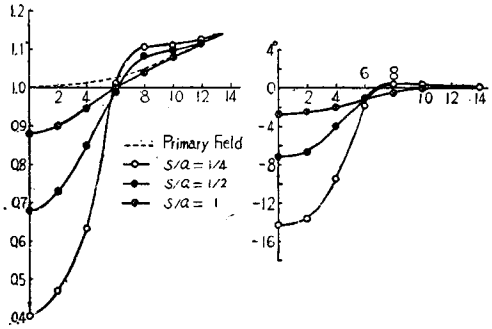

(a) Relative amplitude (b) Phase angle

Fig. 9. Resultant field due to a copper disc of thickness 1 mm ($f = 1{,}000$c/s).

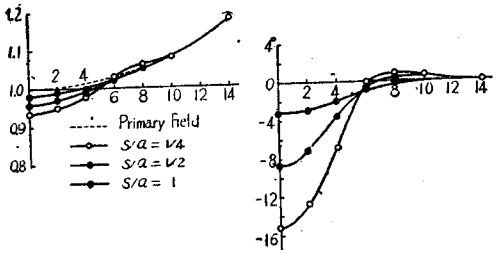

(a) Relative amplitude (b) Phase angle

Fig. 10. Resultant field due to a lead disc of thickness 1 mm ($f = 1{,}000$ c/s).

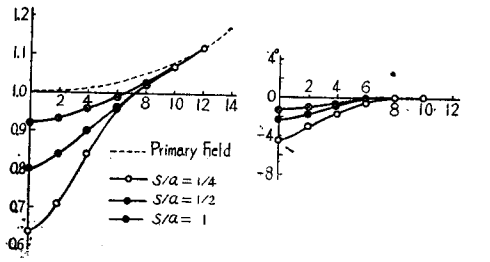

(a) Relative amplitude (b) Phase angle

Fig. 11. Resultant field due to a brass sphere ($f = 1{,}000$ c/s).

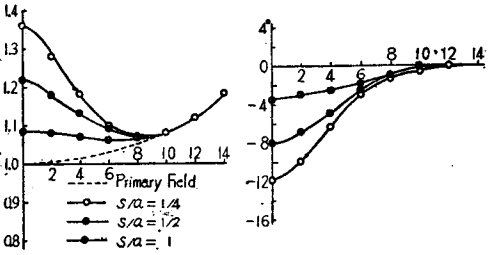

(a) Relative amplitude (b) Phase angle

Fig. 12. Resultant field due to an iron sphere ($f = 1{,}000$ c/s).

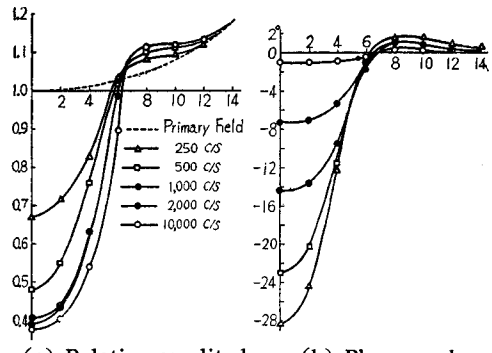

(a) Relative amplitude (b) Phase angle

Fig. 13. Resultant field due to a copper disc of thickness 1 mm ($s/a = 1/4$).

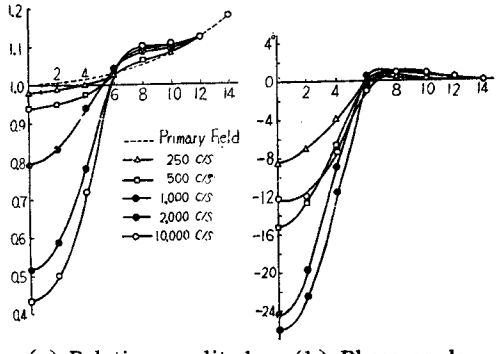

(a) Relative amplitude (b) Phase angle

Fig. 14. Resultant field due to a lead disc of thickness 1 mm ($s/a = 1/4$).

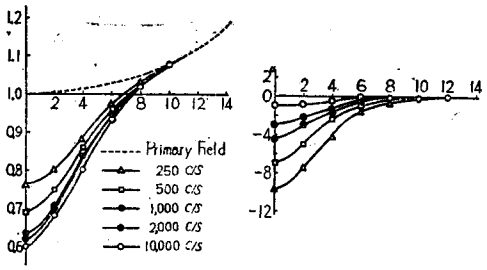

(a) Relative amplitude (b) Phase angle

Fig. 15. Resultant field due to a brass sphere ($s/a = 1/4$).

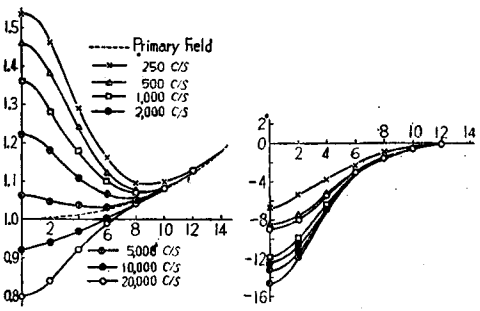

(a) Relative amplitude (b) Phase angle

Fig. 16. Resultant field due to an iron sphere ($s/a = 1/4$).

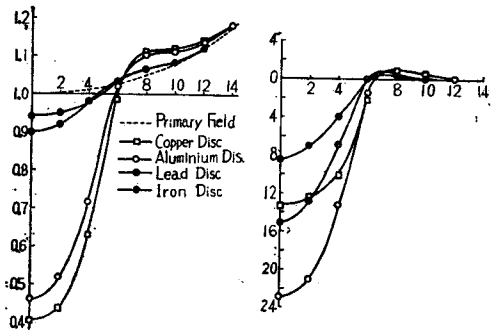

(a) Relative amplitude (b) Phase angle

Fig. 17. Resultant field due to discs of various materials ($f = 1{,}000$ c/s).

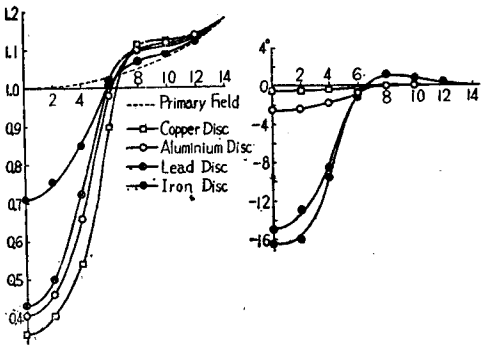

(a) Relative amplitude (b) Phase angle

Fig. 18. Resulant field due to discs of various materials ($f = 10{,}000$ c/s).

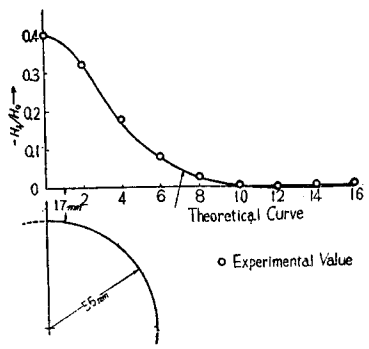

Fig. 19. Vertical component of the secondary field due to a brass sphere.

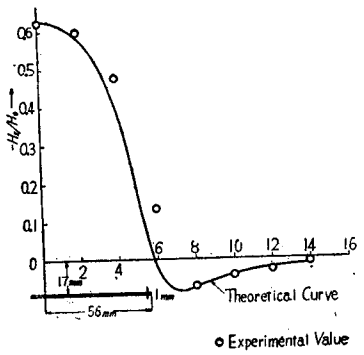

Fig. 20. Vertical component of the secondary field due to a disc.

the center of the sphere, not at the center of the loop, as the average primary field in order to obtain a good agreement between the measured and calculated secondary fields.

In Fig. 20, the experimental values ars taken from the measurement at 10,000 c/s. Some of the discrepancies between these points and the theoretical curve may be due partly to the fact that the measurements are conducted by using a copper disc of 1 mm thickness, whereas the theoretical curve is for a very thin disc of perfect conductor, but it is quite conceivable that they are mainly due to the experimental errors.

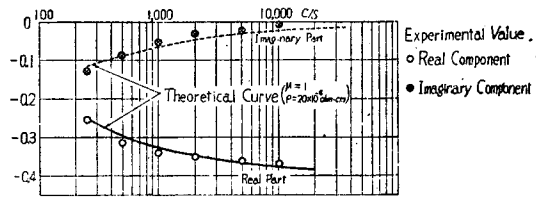

Fig. 21. Real and imaginary parts of the function $Qe^{i\delta}$ for a brass sphere.

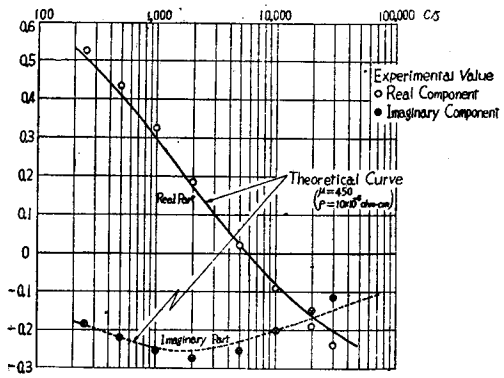

Fig. 22. Real and imaginary parts of the function $Qe^{i\delta}$ for an iron sphere.

Figs. 21 and 22 show the experimental values and theoretical curves of the function X and Y in Eqs. (4) and (5) for brass and iron sphere. It is assumed that the resistivities of brass and cast iron are 20×10^{-6} and $10\times10^{-6}\,\Omega\,\mathrm{cm}$ respectively, and the permeability of cast iron is about 450. By these assumptions, the most of measured points lie on the theoretical curves.

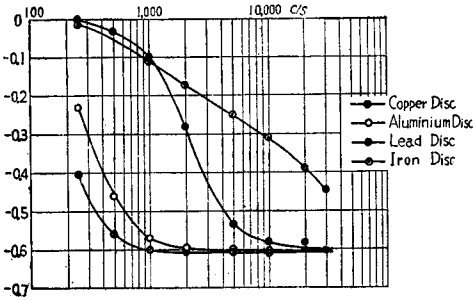

Fig. 23. Real part of the secondary field due to various discs.

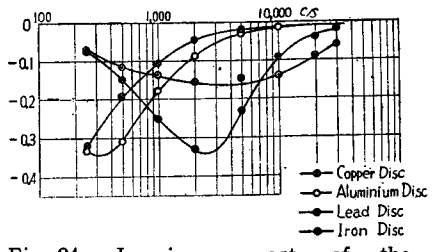

Fig. 24. Imaginary part of the secondary field due to various discs.

Figs. 23 and 24 show the function X and Y for various discs as functions of frequencies. No theoretical expression of the field due to an oblate spheroid of finite conductivity and permeability has been obtained, but the curves shown in these figures are similar to the theoretical curves for $\mu = 1$ in Fig. 3 obtained for spherical conductor.